analytical chemistry

Article

pubs.acs.org/ac

Ion Clouds in the Inductively Coupled Plasma Torch: A Closer Look through Computations

Maryam Aghaei,* Helmut Lindner, and Annemie Bogaerts

Research Group PLASMANT, Chemistry Department, University of Antwerp, Universiteitsplein 1, 2610 Antwerp, Belgium

ABSTRACT: We have computationally investigated the introduction of copper elemental particles in an inductively coupled plasma torch connected to a sampling cone, including for the first time the ionization of the sample. The sample is inserted as liquid particles, which are followed inside the entire torch, i.e., from the injector inlet up to the ionization and reaching the sampler. The spatial position of the ion clouds inside the torch as well as detailed information on the copper species fluxes at the position of the sampler orifice and the exhausts of the torch are provided. The effect of on- and off-axis injection is studied. We clearly show that the ion clouds of on-axis injected material are located closer to the sampler with less radial diffusion. This guarantees a higher transport efficiency through the sampler cone. Moreover, our model reveals the optimum ranges of applied power and flow rates, which ensure the proper position of ion clouds inside the torch, i.e., close enough to the sampler to increase the fraction that can enter the mass spectrometer and with minimum loss of material toward the exhausts as well as a sufficiently high plasma temperature for efficient ionization.

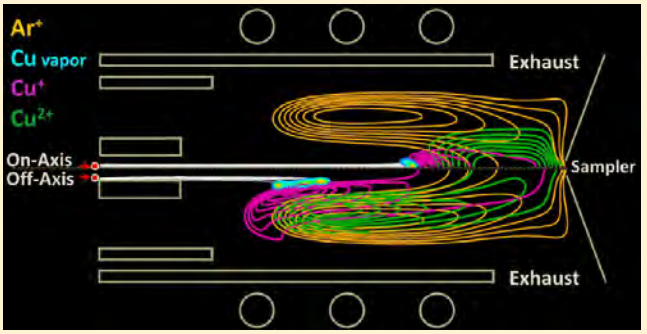

The inductively coupled plasma (ICP) is the most popular ion source in analytical chemistry for elemental mass spectrometry (MS).[1] The sample to be analyzed is introduced with a carrier gas and will undergo several processes such as desolvation, vaporization, diffusion, ionization, and excitation in the plasma. Although, these individual processes are difficult to experimentally measure, several studies have been performed to investigate the material transport through the ICP to improve the analytical capabilities of ICPMS, both experimentally[2−25] and computationally.[26−46]

Hieftje and co-workers introduced isolated, monodisperse droplets of a sample to measure droplet desolvation rates in flames.[2] Later on, Olesik investigated the fate of individual sample droplets in an ICP. He applied a monodisperse dried microparticulate injector (MDMI) and studied the diffusion process of a single element (Sr) after injection of droplets or particles from dried droplets by means of laser-induced fluorescence[3] and side-on optical emission spectroscopy.[4] Kinzer and Olesik[5,6] as well as Lazar and Farnsworth[7,8] observed that the addition of high concentrations of concomitant species leads to a decrease in the number of analyte ions produced from each droplet of the sample solution. Olesik and co-workers also studied the correlations between the number of scattering events from an individual incompletely desolvated droplet and the increase in atom emission intensity and decrease in ion emission intensities.[9] Monnig and Koirtyohann[10] showed that the completion of the aerosol droplet vaporization can explain the transition from the initial radiation zone to the analytical zone of the ICP.

Houk and co-workers[11−14] studied the trajectory and diffusion of analytes during their transport through the ICP. They made a comparison between wet droplets and solid particles by measuring the emission from vapor clouds surrounding the aerosol droplets or particles.[12,13] Several groups also compared the dried solution aerosols from a microconcentric nebulizer with solid particles from laser ablation.[14−16] Moreover, the droplet velocities in the ICP were determined from particle image velocimetry and particle tracking velocimetry.[15]

Niemax and co-workers showed that the spatial positions of analyte atomization and ionization depend on the injector gas flow rate, the droplet diameter, and the amount of analyte.[16−19] This study was performed by means of end-on and side-on optical emission spectroscopy (OES) and applying monodisperse microdroplets (MDMDs). The position of atomization determines the size of the analyte cloud at a particular position. In fact, this is crucial for ICPMS since the size of the analyte ion clouds determines the detection efficiency.

Günther and colleagues investigated the vaporization process of laser-produced aerosols and the subsequent diffusion losses inside the ICP using 2D OES and ICP-quadrupole (Q)MS of individual particles.[20,21] They reported that larger particles may vaporize incompletely or at different axial positions inside the ICP because of composition-dependent melting and vaporization enthalpies.[22] This variable size of atom/ion clouds in front of the MS interface yields nonrepresentative ion extraction.

Received: March 25, 2016
Accepted: July 26, 2016
Published: July 26, 2016

DOI: 10.1021/acs.analchem.6b01189
Anal. Chem. 2016, 88, 8005−8018

It is clear that, in order to optimize the ion transport efficiency through the ICP toward the sampler orifice, several parameters have to be taken into account, such as the size and mass of the analyte droplets, the diffusion rates of the elements studied, the gas flow rates, the applied power, the diameter of the injector inlet, the position of the sampler, as well as the diameter and the pressure drop at the sampler orifice.[23−26] However, the challenge is that these parameters all depend on each other. The effect of the individual parameters can, however, be unraveled by computational investigations, taking into account all important physical processes involved, to support the experimental optimization.

The first model for the "spectrochemical ICP", as a modification of Miller's model[27] was developed by Barnes et al.[28] Miller[27] solved a 2D energy equation with 1D electromagnetic field equations to calculate the 2D temperature field in the torch. Subsequently, Barnes et al.[28] predicted the temperature and velocity fields and the plasma and analyte emission profiles. However, these models did not account for the local cooling of the plasma due to the presence of particles or aerosols. The first model for studying the plasma-particle interaction was developed by Boulos.[29] On the basis of this model, Mostaghimi et al. investigated the flow and temperature fields in the ICP,[30,31] and these simulations were combined with experiments in collaboration with Barnes.[32,33] However, the operating conditions were not always applicable to analytical chemistry purposes and the ICP torch was not connected to a MS interface, so the relevance for ICPMS was limited.

Benson et al. computationally investigated the droplet heating, desolvation, and evaporation in an ICP.[34,35] The total desolvation rate of sample droplets in an argon ICP as well as the trajectories of the particles through the plasma considering droplet−droplet interaction were studied. Horner and Hieftje[36] also studied particle melting, boiling, and vaporization inside the ICP torch, in which particles were assumed to travel along the ICP symmetry axis without significant scatter. However, in all these particle transport modeling studies,[34−36] the initial set of plasma conditions was needed as input by means of a separate code. Therefore, the energy loss by the plasma due to droplet evaporation could not be taken into account because of the separate modeling. Shan and Mostaghimi[37] developed a model to study the plasma behavior within the ICP torch as well as the droplet desolvation and trajectories. In order to determine the droplet trajectories and collisions, a stochastic technique combined with the Monte Carlo method was applied. However, ionization and the presence of the MS interface were not included in this model. Spencer et al.[38,39] presented the first model to describe the effect of the sampler cone in ICP-MS, yet the upstream density and temperature gradients and plasma formation were not included in these models.

The first "self-consistent" model for an atmospheric pressure ICP, operating at typical analytical chemistry conditions, including ionization, was presented by Lindner and Bogaerts.[40] In this model, the transport parameters were for the first time calculated self-consistently for the gas mixture under study, because the above-described models typically apply transport parameters (e.g., viscosity) from the literature. Therefore, the applicability of this model is not limited to specific mixtures for which the data (i.e., species and relative concentrations) are known. Especially the ionization degree is dependent on the actual composition of the plasma, which strongly affects the transport parameters. Note that the transport parameters of the species are adopted from the literature for the pure elements, but in the model, by means of a kinetic model, these input data are used to calculate the corresponding values for the actual composition of the plasma, i.e., a mixture of coper and argon in this study. This makes it possible to apply the model to a wider variety of gas mixtures, including carrier gas and sample material.

Subsequently, we modeled the ICP torch connected to a MS interface cone, considering the large pressure drop from upstream to downstream (i.e., 1 atm to 1 Torr).[41] This model showed for the first time the effect of the presence of a cooled, grounded sampler and of the sudden pressure drop behind it on the plasma characteristics. We performed calculations for a wide range of gas flow rates and applied power and also for various sizes of the injector inlet and sampler orifice.[42,43] In order to optimize the flow behavior inside the ICP torch, recirculation of the gas flow was specifically investigated.[44] Furthermore, a model for elemental particles, where chemical reactions do not play a role, was recently built.[45] This case is relevant for LA-ICPMS, where the sample is injected as ablated elemental particles. The inserted particles were tracked through the ICP torch, up to the evaporation step.[45]

In the present work, for the first time, the ionization of elemental particles is included in the model. Copper particles are taken as a case study and injected from the central inlet. By means of this model, we are now able to track the particles to determine their position, their phase (liquid, vapor, or ionized), velocity, and temperature, both in the ICP torch and at the sampler orifice. More specifically, the shape and position of the ion clouds, originating from the Ar flow as well as from the inserted sample material, are determined inside the torch, which is of interest for emission spectrometry studies as well as for mass spectrometry. With the term "ion cloud" we refer to the sum of the ion clouds from individual particles, which includes both diffusion and the different radial paths that the particles take through the plasma. Note that the model describes the injected material transport up to the sampling cone, but the rest of the ion transport inside the mass spectrometer is not included in the current model. Moreover, as only elemental particles are considered, the model is more applicable to laser ablation (LA)-ICPMS than to ICPMS in general. With this model, any deviation from the central axis as well as any early/late evaporation along the torch are indicated, which are caused by nonoptimal operating conditions. The effects of injection position, applied power, and carrier gas flow rate are studied and the computational results are compared with experimental data from the literature as much as possible, to validate the model and to explain the experimental observations.

COMPUTATIONAL MODEL

The model is a 2D axisymmetric model, based on solving partial differential equations for the gas flow dynamics (i.e., the Navier−Stokes equations), coupled with the energy conservation and Maxwell equations. It is built within the commercial computational fluid dynamics (CFD) program FLUENT 16.0.0 (ANSYS). A validation of this model by experiments was provided in refs 44 and 46. Typical calculation results obtained with the model include the gas flow behavior as well as the plasma temperature and electron density profiles.[41−44] The accuracy of the model is tested in ref 46 by comparing our

DOI: 10.1021/acs.analchem.6b01189
Anal. Chem. 2016, 88, 8005−8018

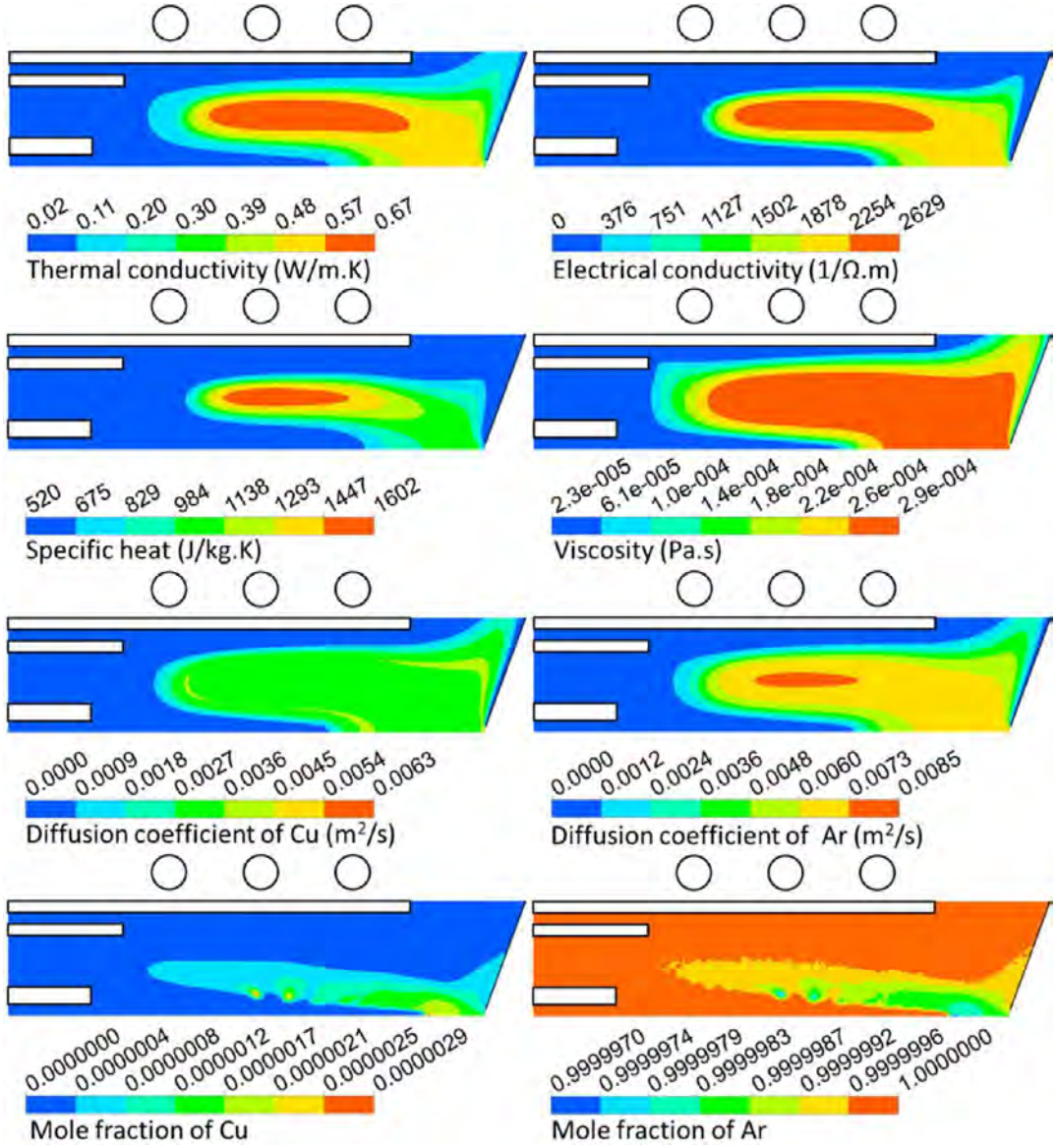

Figure 1. Calculated transport properties of the gas mixture, as well as argon and copper mole fractions, for an applied power of 1400 W and a carrier, auxiliary and cooling gas flow rate of 1.2, 1.2, and 16 L/min, respectively.

calculation results with experimental data. This indicated a deviation of 3% in the temperature. Furthermore, the calculated thermal conductivities are compared with the values obtained from experiments.[47−49] The data are in good agreement (typically less than 5% deviation) for both the pure elements as well as for the example mixture of 50% He and 50% Ar (mole fraction). The maximum deviations reach values of about 10%, which is similar to deviations of the data given in, e.g., ref 50 with respect to ref 49. The deviations appear in the range where significant ionization is present. The exact determination of the uncertainties in the model is, however, not possible, because there are many input data, all with their own uncertainties, but the latter are typically also not known. Because of the huge complexity of the model, the quantitative values should be considered with caution, but we believe that the trends predicted by the model are reliable and that the correct physics and chemistry is captured by the model.

In order to study the material transport through the ICP, the sample introduction is modeled with a so-called "discrete phase model" (DPM).[45] The trajectory of each droplet is calculated by integrating the force balance acting on the particles. Besides their transport throughout the torch, the particles in liquid phase will undergo heating, vaporization, boiling, and finally ionization. For the elemental particles, a heat and mass balance equation is applied, which relates the particle temperature to the convective and diffusive heat transfer and calculates the mass transfer to the vapor phase by means of a vaporization rate based on thermodynamic relations.[45] The heat lost or gained by the particle as it traverses each computational cell also appears as a source or sink of heat in the subsequent calculation of the energy equation in the so-called "continuous phase model" (CPM). Note that the fractal shape of the particles, as well as the radiative heat transfer from the plasma to the particles, is ignored in this calculation.

Once the injected material is in the gas phase, it will be treated as individual atoms in the same way as for the carrier gas, i.e., by solving the Navier−Stokes equations and the Saha−Eggert equation to calculate the ionization degree of the sample

DOI: 10.1021/acs.analchem.6b01189
Anal. Chem. 2016, 88, 8005−8018

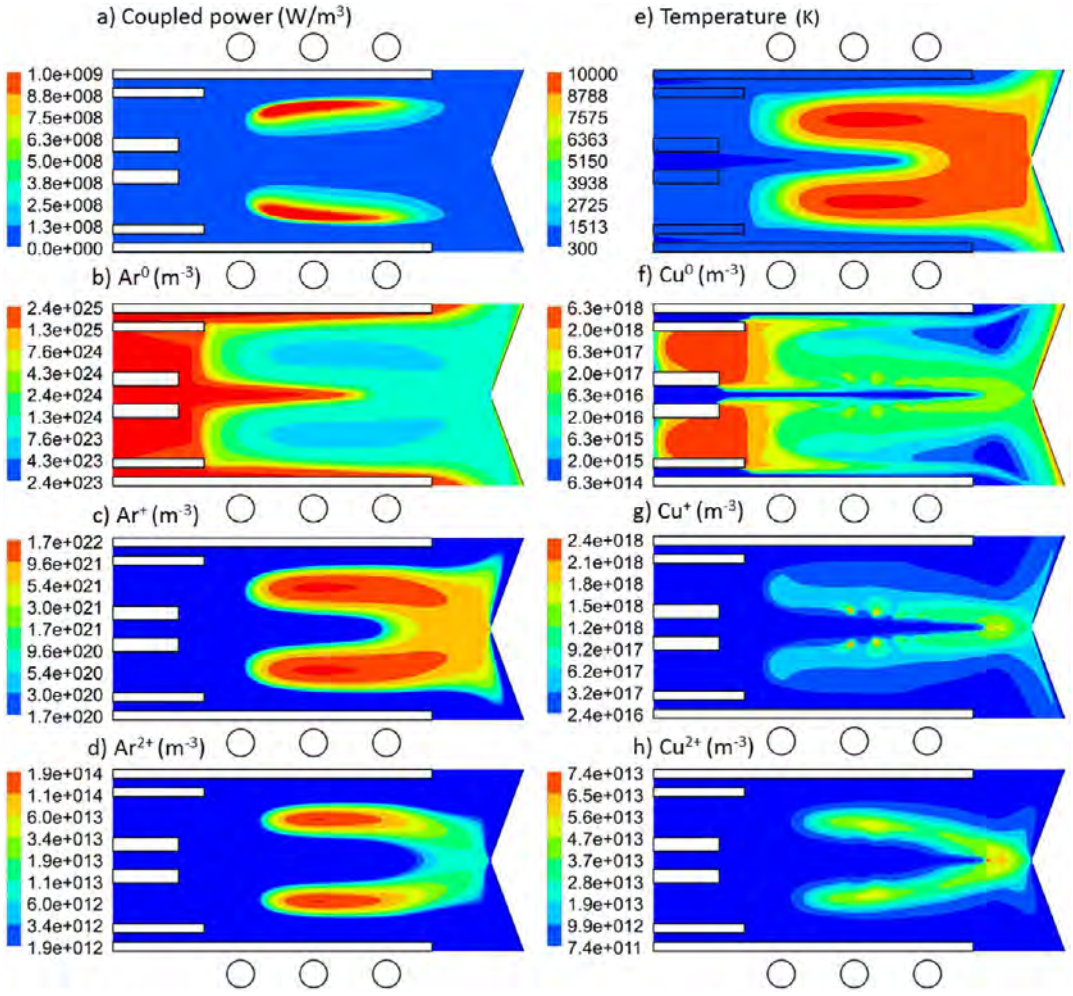

Figure 2. General calculation results of copper droplet introduction, with diameter of 1 μm and flow rate of 100 ng/s injected from the whole width (2 mm) of the central inlet, for an applied power of 1400 W and a carrier gas flow rate of 1.2 L/min: 2D profile of (a) coupled power density, (b–d) Ar^0, Ar^+, and Ar^{2+} number density, (e) plasma temperature, (f–h) Cu^0, Cu^+, and Cu^{2+} number density.

material at the local plasma temperature, assuming local thermodynamic equilibrium (LTE). From the ionization degree and the (mass and charge) conservation equations, the number densities of electrons and of the atoms and ions of the sample material can be calculated. It is justified to apply the LTE condition to the plasma. A direct comparison between simulation and experiment was performed, as discussed in detail in ref 46. By means of end-on ICP optical emission spectroscopy, we collected the light from different areas in the plasma and compared it with the simulation results. The plasma temperature inside the central channel was experimentally determined from the end-on collected line-to-background ratio. The calculated and measured values for the plasma temperature were found to be in good agreement (i.e., within 3% deviation). In fact, the plasma is operating at atmospheric pressure. Thus, characteristic collision times are in the order of 10 ps, while one period of the rf-field takes a few ten nanosecons. Thus, on the order of 1000 collisions with atoms taking place per electron during one oscillation of the rf field. In contrast to dc discharges, electrons do not gain energy on average if they do not undergo collisions since the oscillating electric field accelerates and decelerates them in the same way during one period. This means that close-to LTE conditions can be achieved. Although the assumption of LTE is not fully correct, the use of a two-temperature model does not necessarily yield significantly different temperatures for electrons and heavy species.[51] Therefore, we believe that the assumption of LTE is quite comparable to the accuracy of non-LTE models for the present plasma. LTE, in particular, has the advantage that the model can be more easily formulated consistently and it requires less other assumptions (e.g., on power coupling and energy transfer from electrons to atoms and ions) and/or (sometimes imprecise) parameters. Using the capabilities of LTE simulations for thermochemical processes in an ICP, Pupyshev et al.[52] calculated the formation efficiencies of singly and doubly charged ions of 84 elements within the temperature range of 4000–10 000 K by steps of 500 K, which showed good agreement with experimental data. Moreover, a two-temperature computational model[53] for an rf ICP torch, applied to monatomic gases, indicated that deviations from LTE were relatively small at atmospheric pressure, i.e., within ~5% for the bulk plasma, up to ~10% for the areas close to the torch walls, but at reduced pressure substantial deviations from LTE were noted, i.e., ~20–30%. As the present model is applied to atmospheric pressure, we believe the LTE approach is sufficiently valid.

The ionization model is added to FLUENT as a self-written code. For any injected material, several material parameters are

DOI: 10.1021/acs.analchem.6b01189
Anal. Chem. 2016, 88, 8005–8018

needed, both in liquid and gas phase. Some parameters, i.e., the viscosity, thermal conductivity, and diffusion coefficients, are a function of the local gas composition and plasma temperature and are again inserted in the model as self-written codes. The plasma species considered in the model are atoms, singly and doubly charged ions for Ar and Cu, as well as electrons. The diffusion coefficient of copper particles (up to evaporation) in Ar gas is adopted from ref 54 as a function of temperature. More details about the calculation of the transport properties are provided in refs 40 and 45. Figure 1 shows the thermal and electrical conductivity, specific heat, viscosity, diffusion coefficients of Cu and Ar, and the Cu and Ar mole fractions, as calculated for the actual temperature and gas composition inside the entire torch, at 1400 W power and 1.2, 1.2, 16 L/min flow rate of carrier gas, auxiliary gas, and cooling gas, respectively. To implement the DPM into the CPM of the ICP, a FLUENT model is built including the injection properties, material parameters, and the physical models applicable for elemental particles. After obtaining convergence for the Ar plasma properties, we introduce the particles. In each iteration, the exchange of mass, momentum and energy between plasma and particles is calculated and both the DPM and CPM are updated. Finally, the ion clouds are tracked along the torch, providing also information on the number density of each species at the sampler orifice, which yields the transport efficiency of elemental particles.

Note that in order to apply the DPM to our calculations, the introduced sample needs to be in a fluid phase, either liquid or gas. Therefore, in this work, we introduce pure copper material using liquid injection, but the particles are introduced at room temperature and the transport properties are calculated based on the temperature of the Ar flow. Therefore, the particles are treated with the transport properties of first solid phase (300−1357 K) and then liquid phase (>1357 K). In other words, "quasi-particles" are introduced and carried with the gas flow, up to reaching the vaporization point. It should be realized that, because the particles are introduced in liquid phase, the energy exchange at melting point is not included. This assumption is justified, because the latent heat of melting for copper (203.5 kJ/kg) is much smaller than the latent heat of vaporization (5310 kJ/kg) and melting can thus be ignored in our calculations, while the quasi-particles still undergo heating, starting from room temperature, i.e., as solid phase. Note that in the rest of the manuscript, we will simply call them "particles".

RESULTS AND DISCUSSION

General Calculation Results. All calculation results will be illustrated for copper particles with a diameter of 1 μm, inserted at the central inlet with 2 mm width, at a flow rate of 100 ng/s. They are tracked through the torch up to the sampler position (i.e., 41.5 mm distance from the central inlet). The total applied power is varied between 600 and 1600 W and the carrier gas flow rate ranges between 0.4 and 1.6 L/min. The auxiliary and cooling gas flow rates are kept at 1.2 and 16 L/min, respectively.

Figure 2 shows the 2D profiles of coupled power density and temperature inside the plasma (a,e) as well as of the argon and copper species number densities, i.e., Ar, Ar^+, and Ar^{2+} (left column; b,c,d), and Cu, Cu^+, and Cu^{2+} (right column; f,g,h) for an applied power of 1400 W and a carrier gas flow rate of 1.2 L/min, which are typical conditions of interest for ICPMS.[55] We showed before[45] that a mass loading flow rate up to 100 μg/s has only a minor effect on the plasma temperature profile. Therefore, the plasma temperature shown in Figure 2d is almost the same as for pure Ar (see, e.g., ref 44), as we use a mass loading flow rate of 100 ng/s for pure copper particles in this study. This value is based on laser ablation studies and taken from experimental values of femtosecond-laser ablation of copper cells for a long washout time.[56] For aqueous analyte solutions, feed rates up to 0.1 g/min (or 1.7 mg/s) are used, and even for these flow rates, it was reported that the plasma temperature is not affected by the sample introduction.[16−18]

The species number density profiles shown in Figure 2 are plotted on a logarithmic scale, and not in the same scale, in order to clearly show the maximum values of each species inside the torch. It is clear that most of the argon ionization takes place in the coil region, where the external power is mostly coupled to the gas flow and the maximum temperature is reached, see Figure 2a,c−e. In the case of copper ionization, the maximum is closer to the central axis, as the copper ionization potential is much lower than that of argon (i.e., 7.73 eV vs 15.76 eV) and the ionization can thus take place at lower temperature.

Looking at the absolute values, it is clear that the Ar gas atoms are by far the most abundant (Figure 2b). Their number density when entering the torch is 2.4×10^{25} m^{-3}, corresponding to atmospheric pressure and room temperature. However, inside the plasma, their number density drops to around 6×10^{23} m^{-3} due to the high temperature, and its volume integrated value over the entire torch is 7.9×10^{24} m^{-3}. The Ar^+ ion number density (Figure 2c) reaches a maximum of 1.7×10^{22} m^{-3}, with a volume integrated value over the entire torch of 2.6×10^{21} m^{-3}. This indicates that the ionization degree of Ar, at the position of maximum ionization (i.e., the position of maximum power coupling and maximum temperature, i.e., 10 200 K) is about 2.8%. This is in reasonable agreement with the calculated results from ref 52, where the ionization degree at 10 000 K for argon is stated to be 2.08% and at 9500 K as 1.20%. However, integrated over the entire torch region, the ionization degree of the Ar gas is about 0.033%. The maximum Ar^{2+} ion number density (Figure 2d) is only about 1.9×10^{14} m^{-3}, hence 8 orders of magnitude lower than the maximum Ar^+ ion number density. Thus, a negligible fraction of the Ar^+ ions is further ionized into Ar^{2+} ions. This is logical, because of the high second ionization potential of Ar (i.e., 27.7 eV). Although the doubly charged ions are negligible in terms of total composition of the plasma, they still might be significant enough to be detected. Moreover, when low concentrations of analyte are being measured, these signals reduce the analytical signals from elements at the same mass per charge ratio and cause spectral interferences in ICPMS.[57] The number density profile of the Cu atoms (Figure 2f) can be explained from the evaporation process and the Ar gas flow path lines, as illustrated in Figure 3. In this figure the trajectory of the three Ar gas flows originating from the central, intermediate, and outer inlets are plotted in black, violet, and orange, respectively. The mass transfer rate of the Cu particles to the gas phase is also shown and indicates that the copper particles do not all evaporate at the same radial and axial position (see separate regions of maximum mass transfer rate). The Cu particles injected from the outer region of the inlet (also called "off-axis") follow different path lines of the Ar gas flow than the ones which are injected from the central region of the inlet. Indeed, the particles injected "off-axis" move away from the central axis, and they experience the hotter regions in

DOI: 10.1021/acs.analchem.6b01189
Anal. Chem. 2016, 88, 8005−8018

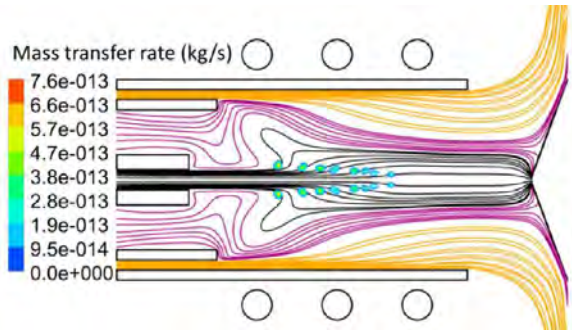

Figure 3. 2D profile of the mass transfer rate of copper droplets to the gas phase, as well as 2D trajectories of the Ar gas flows originating from the central (black), intermediate (violet), and outer (orange) inlets.

the plasma earlier and therefore start to evaporate earlier, while the ones that stay on axis, go more straight and will evaporate more downstream of the torch. A detailed discussion about the Ar path lines, their radial expansion, and backward motion can be found in refs 41, 44, and 45.

As a result of the different positions of Cu evaporation, two maxima can be observed in the Cu atom density profile of Figure 2f. The initial source of atomic Cu is close to the central axis, where the evaporation takes place (see Figure 3), and therefore some "local maxima" (light green contours) are observed near the end of the cool central channel. However, because of the diffusion of Cu atoms into the Ar flow, and following the path lines of the auxiliary gas flow (see Figure 3), the Cu atoms also expand in the torch with the backward motion of the Ar gas flow. As a consequence, the maximum Cu atom density (around 6.3×10^{18} m^{-3}) occurs close to the inlets, due to the backward motion of the gas flow, at the same place as for the Ar atom density. The plasma temperature is here near room temperature, so ionization does not take place. From this region, the Cu atoms are carried by the cooling gas to the outer exits of the ICP or by the auxiliary gas to the center and toward the sampler.

The Cu atom number density, volume integrated over the entire torch, is 1.13×10^{18} m^{-3}. This indicates that the Cu atoms are more than 6 orders of magnitude less abundant than the Ar gas atoms in the plasma. At higher mass loading flow rates, this ratio will of course increase accordingly. In spite of this much lower Cu density, the Cu^+ and Cu^{2+} ions are not so much less abundant than the Ar^+ and Ar^{2+} ion densities, as is illustrated in Figure 2g,h. At the central axis, the Cu^+ and Cu^{2+}

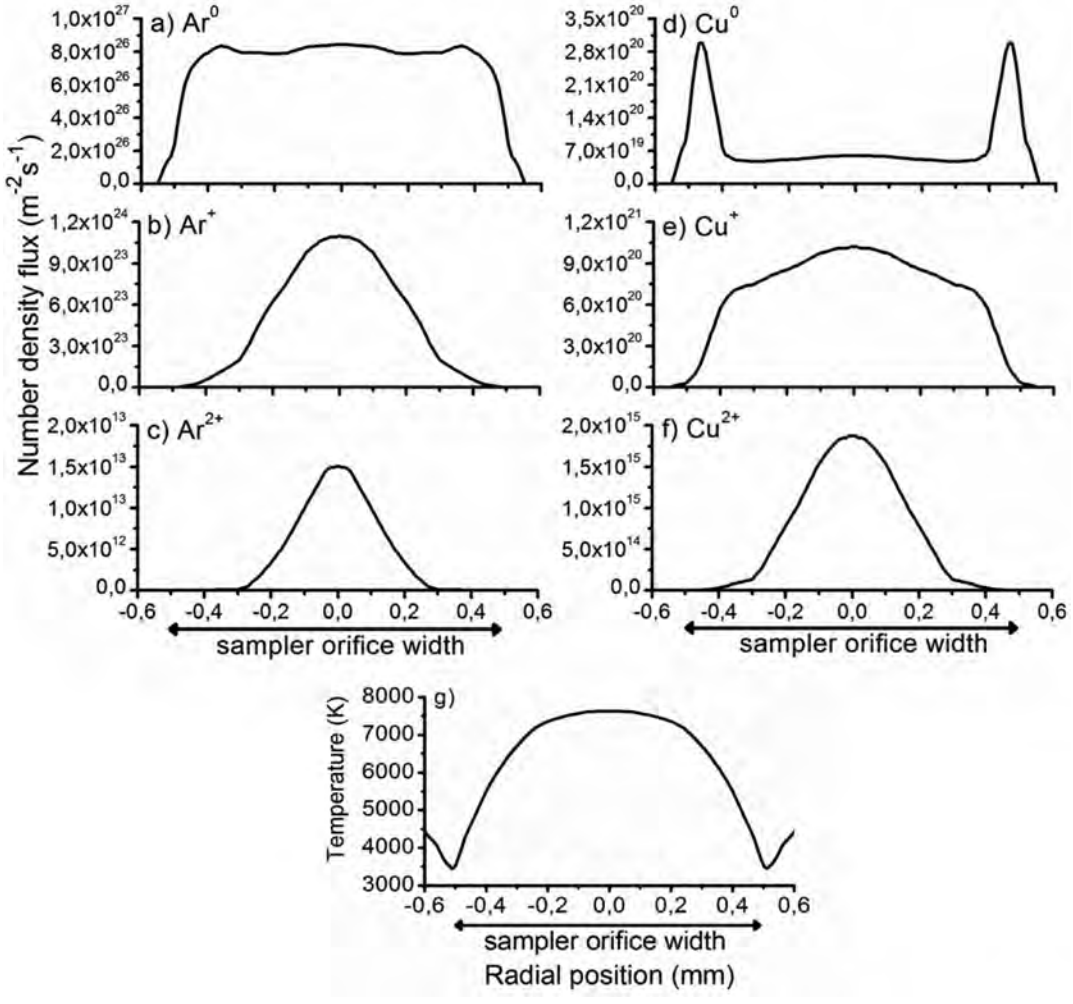

Figure 4. Fluxes for (a) Ar^0, (b) Ar^+, (c) Ar^{2+}, (d) Cu^0, (e) Cu^+, and (f) Cu^{2+} and (g) temperature at the sampler orifice as a function of radial position.

DOI: 10.1021/acs.analchem.6b01189
Anal. Chem. 2016, 88, 8005−8018

ions reach their maximum density near the sampler, but they also show a second maximum in the region of maximum coil power and maximum temperature, like in the case of Ar. The maximum Cu^+ ion density is about 2.4×10^{18} m^{-3} (see Figure 2g), and their volume integrated density is 1.4×10^{18} m^{-3}. Hence, the overall ionization degree of Cu, integrated over the entire torch region, is about 55%. This is much higher than in the case of Ar, which is logical, due to the lower ionization potential (see above). Furthermore, in the regions of maximum Cu^+ ion density (i.e., where a maximum temperature of 10 200 K is reached), the local ionization degree is calculated to be more than 90%. This is again in agreement with the calculated results from ref 52, where the ionization degree at 10 000 K for copper is stated to be 91.8% and at 9500 K as 91.7%. The exact comparison is not possible because in ref 52, the injected analytes are diluted in water. The maximum Cu^{2+} ion density is about 7.5×10^{13} m^{-3}, and the volume integrated density is around 3×10^{13} m^{-3} (see Figure 2h). This indicates that only a small fraction (i.e., about 0.002%) of the Cu^+ ions is further ionized into Cu^{2+} ions. Although this fraction is still very low, it is about 2000 times higher than for Ar, which can again be explained from the lower second ionization potential of Cu (i.e., 20.9 eV).

Figure 2 indicates that both the atom and ion clouds of both Ar and Cu can reach the sampler but also that some parts of these clouds will also exit through the exhausts (i.e., open sides) of the torch. By comparing Figure 2g,h, we can deduce that the Cu^{2+} ions are all evacuated through the sampler orifice, while some of the Cu^+ ions exit through the exhausts of the torch. However, because of the drop in temperature at the exhausts, they will recombine again to the atomic phase; for more details, see Figure 5 below.

Thus, we can summarize the steps from Cu particles to Cu vapor and to the Cu^+ and Cu^{2+} ions as follows, using copper just as an example of any elemental sample. The Cu particles are inserted from the central inlet and carried by the Ar flow until they start to evaporate (blue contours in Figure 3), atomize (Figure 2f), and ionize (Figures 2g and 1h, for single and double ionization, respectively). These figures illustrate to what extent the clouds of each species expand in the torch. This might be useful for both emission and mass spectrometry. Any displacement in the radial or axial position of the ion clouds can change the number of ions reaching the sampler orifice, which will effect the ion signals in the MS. Likewise, for optical emission spectrometry, the ion signals are very sensitive to the exact position at which the data are obtained.

In Figure 4 we show the calculated fluxes of the Ar and Cu atoms and ions at the position of the sampler orifice, as a function of radial distance from the central axis, at the same conditions as in Figure 2, as well as the temperature profile. At the bottom of the figure, the width of the sampler orifice is indicated for clarity. In general, the ion fluxes reach a maximum at the center of the sampler orifice, corresponding to the axial velocity of the flow which reaches its maximum (~900 m/s) at the center of the sampler and drops toward the edge of the sampler cone, i.e., 0.5 mm from the central axis. Moreover, in the region near the sampler, the ionization reaches its maximum at the central axis, where the temperature is slightly higher. The latter can be explained by the cooling effect of the sampler, which has an orifice of 1 mm diameter. For the same reason, the atom fluxes reach their maximum at the radial position corresponding to the orifice diameter (see Figure 4). This is most apparent for the Cu flux, as it reflects the position where most of the Cu particles (i.e., on-axis, near the sampler) are vaporized. However, the atomic fluxes do not reach a minimum at the center of the sampler, because of the maximum flow speed in this region. Details of the velocity profiles of the Ar flow can be found in ref 41. The absolute values of the copper species fluxes in the central 1 mm (i.e., within the sampler orifice width) show how many of these species can enter the MS interface per second. At the conditions of Figure 4, the total (i.e., radially integrated) fluxes of the Cu atoms, Cu^+ ions, and Cu^{2+} ions are about 7×10^{19} $m^{-2}s^{-1}$, 7×10^{20} $m^{-2}s^{-1}$, and 7×10^{14} $m^{-2}s^{-1}$, respectively.

Effect of Injection Position, Power, and Carrier Gas Flow Rate on the Sample Transport Efficiency from Inlet to Sampler. In this section, we compare the fluxes of ions passing through the sampler (by integrating the values over the entire orifice width) with the sample flux entering the torch at the inlet. This allows us to calculate the transport efficiency of the sample material from the inlet until entering the MS interface at different operating conditions. Specifically, we study the effect of injection position at the central inlet, applied power and carrier gas flow rate, and we show that these parameters determine the position of the ion clouds inside the torch, which affects the fluxes at the sampler orifice, and thus the sample transport efficiency.

Effect of Injection Position. In the previous section, we introduced the copper particles from the entire width of the central inlet. To study here the effect of the injection position, we introduce the same amount of copper particles (100 ng/s with a diameter of 1 μm) from two different initial positions at the entrance, i.e., on-axis and off-axis. The other operating conditions are kept the same as in Figure 2. Figure 5a shows the 2D Cu^+ ion number density profile for on-axis injection (more specifically within 0.25 mm width from the center of the inlet; upper frame) and off-axis injection (i.e., within 0.25 mm from the side wall of the inlet; bottom frame). The particle tracking

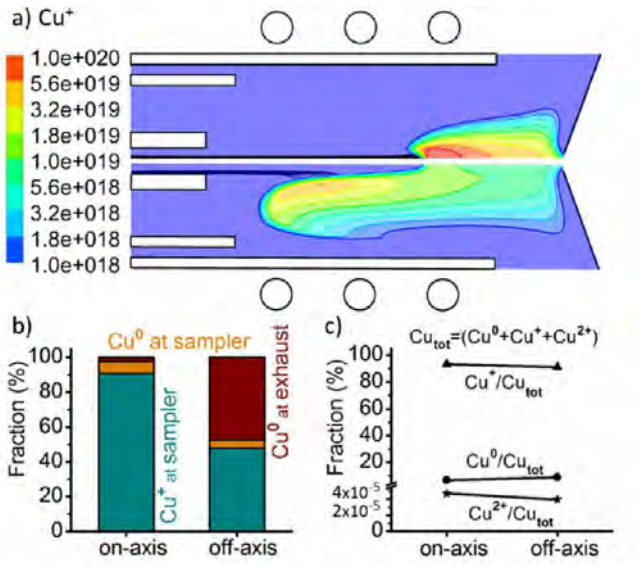

Figure 5. (a) 2D profile of Cu^+ number density for on-axis (upper frame) and off-axis (bottom frame) injection as well as particle tracking of the copper droplets (brown path lines), (b) fraction of Cu^0 and Cu^+ at the sampler and fraction of Cu^0 leaving at the exhausts of the ICP, with respect to the total amount of Cu at the inlet, (c) fractions of Cu^0, Cu^+, and Cu^{2+} at the sampler orifice, with respect to the total amount of Cu passing through the sampler.

DOI: 10.1021/acs.analchem.6b01189
Anal. Chem. 2016, 88, 8005−8018

of the Cu particles is also plotted in black path lines. For the sake of comparison, only one-half part of the torch is shown for each case in Figure 5a. It can be seen that the particles which are injected on-axis move more forward in a straight line throughout the torch, while the ones which are off-axis injected deviate from the central axis at an earlier axial position. Therefore, the ion cloud in the upper frame of Figure 5a is found more on the central axis and expands less, while the ion cloud in the bottom frame shows a broader expansion along the torch.

In Figure 5b, the calculated fractions of Cu^0 atoms and Cu^+ ions entering the sampler orifice as well as the fraction of Cu^0 atoms exiting through the exhausts of the ICP torch, with respect to the total amount of Cu entering the torch at the inlet (i.e., 100 ng/s), are plotted both for on-axis and off-axis injection. Cu^+ is of course the most important species, as Cu^0 cannot be detected in the MS. The fractions of Cu^{2+} ions are not indicated, as they are 4.5×10^{-5} and 2×10^{-5} for on-axis and off-axis injection, respectively, and thus negligible compared to the other species. The effect of injection position on the transport efficiency through the sampler is quite evident. When all the droplets are injected on-axis, the dominant fraction (around 90.6%) will pass through the sampling cone in the form of Cu^+ ions, while about 6.8% of the material passes as Cu^0 atoms through the sampler, and 2.6% exits through the exhausts. However, in the case of off-axis injection, only 48% of the injected material will enter the MS interface as Cu^+ ions, while almost the same fraction (47%) leaves the ICP through the exhausts and 5% passes as Cu^0 atoms through the sampler. This clearly demonstrates that any deviation of the injected material from the central axis will lead to a loss of intensity in the MS, which should be avoided. Indeed, the radial movement of the sample particles to the outer region of the torch lowers the chance that the sample can pass through the sampler cone. Hence, the detection efficiency becomes lower, as some part of the sample is lost in the torch (i.e., it will leave the ICP through the exhausts) and is not effectively sampled through the plasma−vacuum interface. This suggests that using smaller injector inlets will be beneficial, especially for laser ablated particles, as indeed observed experimentally in ref 18. To our knowledge, this is the first time that a model for ICPMS can calculate the amount of ions at the sampler orifice and predict optimum operating conditions for this purpose (see below).

The early evaporation of samples due to deviation from the central axis affects the ion density not only upstream but also downstream the sampler. The groups of Farnsworth and Spencer studied the velocity profiles of the argon flow entering the MS vacuum stages, by means of experiments and computations, respectively, and also concluded that any deviation of analyte from the central axis affects the transmission between the first and second vacuum stages. In fact, the gas flows passing through the sampling cone off-axis, will expand off-axis in the first vacuum stage and therefore they get lost in the skimming process.[25,38,39,58] Again, our simulations suggest that using a smaller inlet will be beneficial to avoid these losses.

Figure 5c shows the copper species fractions at the sampler orifice for on-axis and off-axis injection, by integrating the fluxes of the Cu^0 atoms, Cu^+ and Cu^{2+} ions on the sampler orifice surface. The dominant species in both cases are Cu^+, with a fraction above 90%, being slightly lower in the case of off-axis injection. The Cu^0 atoms have a fraction of about 7% for both on-axis and off-axis injection, while the fraction of Cu^{2+} is only in the order of 10^{-5} %.

Effect of Applied Power. Figure 6a illustrates the effect of applied power, ranging from 600 to 1600 W, on the calculated

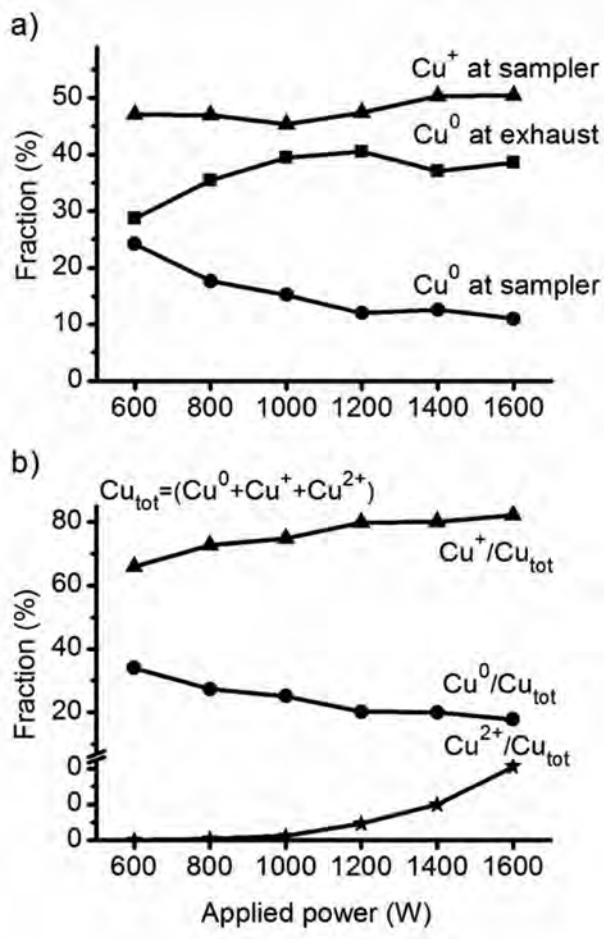

Figure 6. (a) Fraction of Cu^0 and Cu^+ at the sampler and fraction of Cu^0 leaving at the exhausts of the ICP, with respect to the total amount of Cu at the inlet, and (b) fractions of Cu^0, Cu^+, and Cu^{2+} at the sampler orifice, with respect to the total amount of Cu passing through the sampler, for different applied powers.

fractions of Cu^0 atoms and Cu^+ ions entering the MS sampling cone as well as the fraction of Cu^0 atoms exiting through the exhausts of the ICP torch, with respect to the total amount of Cu entering the torch at the inlet (i.e., 100 ng/s), for a fixed carrier gas flow rate of 1.2 L/min and assuming that the Cu sample is injected from the entire central inlet (i.e., no distinction between on-axis and off-axis). The fraction of Cu^{2+} ions is again not shown, because it is on the order of 10^{-7}–10^{-5}, although increasing with power. Similar to Figure 5b, the sum of the three curves in Figure 6a is always equal to 100%, as the total amount of Cu in the torch, either as Cu^0 atoms or Cu^+ ions (and Cu^{2+} ions) must either leave the torch through the sampler orifice or through the exhausts.

The fraction of Cu^0 which enters the MS interface through the sampler orifice decreases from 25% to 10% upon increasing the applied power, while the fraction of Cu^+ ions entering the MS interface (around 50%) first slightly decreases up to 1000 W and then slightly increases. The fraction of Cu^0 atoms leaving the torch through the exhausts (about 30−40%) first

DOI: 10.1021/acs.analchem.6b01189
Anal. Chem. 2016, 88, 8005−8018

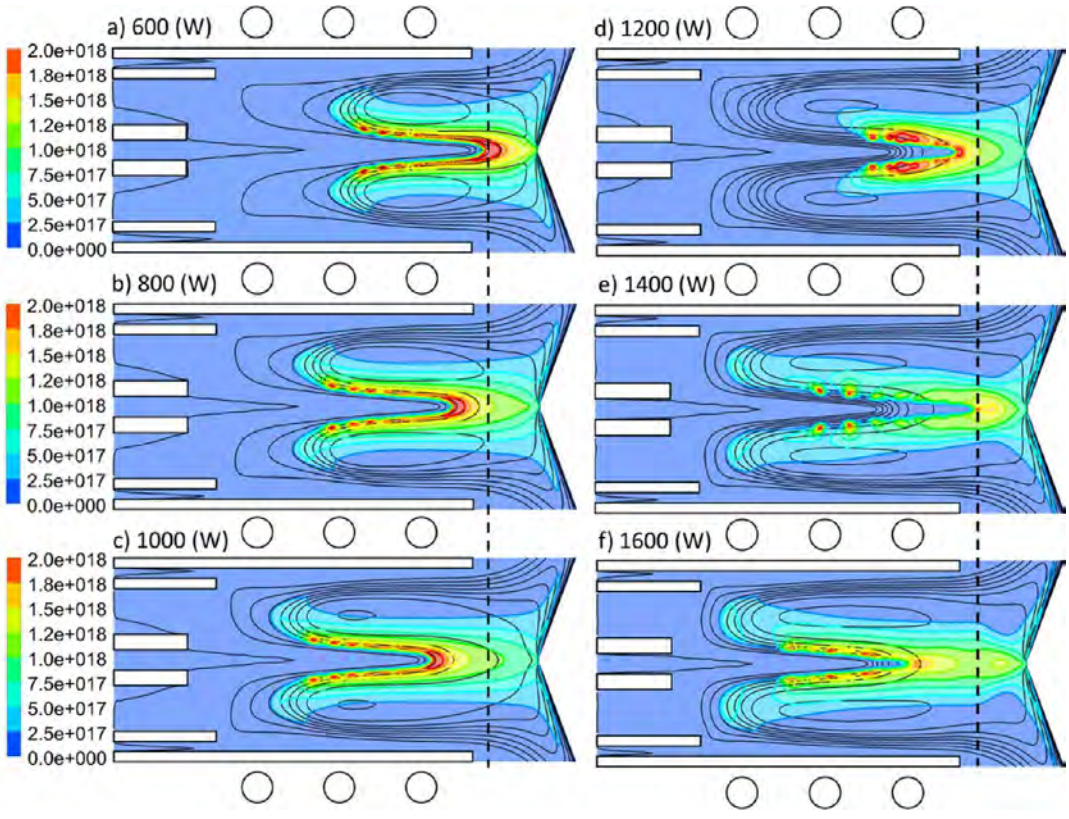

Figure 7. 2D profiles of Cu^+ number density at different applied power of (a) 600, (b) 800, (c) 1000, (d) 1200, (e) 1400, and (f) 1600 W, as well as plasma temperature profiles (black contours) ranging from 300 to 10 000 K.

slightly increases and then stays more or less constant. The most important result from this figure is that about 50% of the injected copper will pass through MS interface as Cu^+ ions. This transport efficiency of 50% is comparable to the result of Figure 6b for off-axis injection, which is quite logical because in reality, overall only a minor fraction of the sample is really injected on-axis. However, this also suggests that one should be able to improve the detection efficiency by using a narrower central gas inlet, where all the sample is injected close to on-axis.

In Figure 6b the copper species fractions at the sampler orifice are depicted for different applied powers. At all applied powers investigated, the majority of the Cu entering the MS interface will be Cu^+ ions. This fraction is 66% at a low applied power of 600 W and 82% at a high power of 1600 W. However, note that this corresponds only to about 50% of the injected Cu from the inlet, according to Figure 6a. The Cu^{2+} ions form only a very minor fraction of the amount of Cu passing through sampling cone. By increasing the applied power, the ion fractions at the sampler increase, while the fraction of Cu^0 atoms decreases. We showed in ref 42 for a pure Ar flow that at a fixed carrier gas flow rate, increasing the applied power inside the torch leads to a rise in the plasma temperature and therefore also in a rise in the ionization rate and thus in the ion number densities and fluxes.

In order to study the changes caused by the power in more detail, we plot in Figure 7 the 2D profiles of the Cu^+ ion number density (in color) as well as the contour lines of the plasma temperature (plotted in black, in the same scale as Figure 2e for the different cases, ranging from 300 K to 10 000 K), for 6 different values of applied power, i.e., from 600 to 1600 W. The carrier gas flow rate is again kept at 1.2 L/min. The temperature profiles are just added for illustration and to assist in the explanation, but they were discussed in more detail in our previous work[42] for pure Ar. Since the copper particle flow rate is 10 orders of magnitude lower than the Ar flow rate (i.e., 100 ng/s corresponds to only 8.36×10^{-10} L/min), the temperature profiles are unaffected upon addition of the Cu particles, as discussed above and in refs 16−18, 41, and 45.

The general trend of increasing the applied power is a drop in the length of the cool central channel (see the black contours). Indeed, at 600 W, the temperature at the central channel is below 1300 K up to a distance of 34.8 mm from the injector inlet, while at 1600 W, it starts rising already at a distance of 25.7 mm. This is quite logical and was also illustrated in ref 42. It means that the sample vaporization can take place earlier in the torch at higher power. The same behavior was also found experimentally. Indeed, Blades et al.[23] and Chan and Hieftje[24] performed OES on ICPs loaded with dispersed liquids and reported that an increase of the rf power raises the ICP gas temperature and made particles vaporize earlier. Horner et al.[26,36] as well as Shan and Mostaghimi[37] reported from their modeling studies that the height of complete desolvation decreases fairly linearly with an increase of the applied rf power.[37] Finally, also Mills et al.[25] reported that a higher power causes a shift in atomization and ionization toward the load coil, based on planar laser-induced fluorescence to map the density distributions in the region between the load coil and the sampler.

Besides the axial shift in sample vaporization to earlier positions in the torch, causing also the ionization to take place earlier in space, a narrowing of the Cu^+ number density profile in the radial direction upon increasing power can also be observed from Figure 7. A similar trend was also evident in the

DOI: 10.1021/acs.analchem.6b01189
Anal. Chem. 2016, 88, 8005−8018

fluorescence images reported in ref 25 at a position of 5 mm downstream from the load coil and 5 mm upstream from the sampler. This behavior can be explained as follows: As the copper is introduced here from the whole width of the central inlet and not only on-axis, we see that the ion clouds are formed in a relatively wide area (i.e., not only on-axis). Therefore, the maximum ionization occurs at different places along the torch, depending on the exact injection position. Indeed, the particles introduced near the outer sides of the inlet (i.e., off-axis) are ionized earlier in the torch for all the cases in Figure 7, because they expand somewhat more in the radial direction, following the Ar gas path lines, and therefore they reach the hotter areas in the coil region earlier, where they will evaporate and ionize. Thus, the off-axis ion clouds are shifted upstream the load coil upon increasing power, due to the correspondingly higher temperatures, and therefore, the off-axis maxima occur earlier in the torch and the density near the sampler drops. This is the reason why the ion clouds become narrower and are located earlier in space upon increasing the applied power. Furthermore, for the particles introduced near the center of the inlet (on-axis), an increase in power from 600 to 1000 W (left column) also leads to an upstream shift of the central ionization maximum, following the temperature profile (black contours). The vertical black dashed line indicates the maximum in Cu^+ ion density at 600 W and thus shows how this maximum is shifted away from the sampler. This explains the slight drop in Cu^+ fraction at the sampler from 600 W to 1000 W, presented in Figure 6a. However, in the right column of Figure 7, we see that further increasing the power does not yield the same reduction in the length of the central channel as in the lower power range. Note that the length of the central channel is defined in our study based on the two lowest temperature contours. However, the high temperature area again shifts more to the sampler (see black contour lines), so that the maximum of the ion number density also takes place closer to the sampler (see Figure 7d). In Figure 7e,f, the maximum ion density is off-axis and in the coil region, originating from the particles injected off-axis, but a secondary maximum, albeit smaller, is indeed moving closer to the sampler. Hence, these profiles, and especially the region near the sampler, explain why the flux of the Cu^+ ions is relatively high at 600 W, followed by a small drop until 1000 W, and again a slight increase toward the two highest powers investigated, as observed in Figure 6a above. Therefore, in the following we will keep the power fixed at 1400 W for studying the effect of the carrier gas flow rate.

Effect of Carrier Gas Flow Rate. We already showed that for any specific injector inlet diameter, there is a transition flow rate for the carrier gas below which the central channel does not occur.[46] The transition flow rate for the inlet diameter of 2 mm which is used in this study is 0.4 L/min. Therefore, we chose 0.4 L/min as the lowest flow rate and studied the effect of carrier flow rate up to 1.6 L/min. In Figure 8, we show the fractions of Cu^0 atoms and Cu^+ ions at the sampler and of Cu^0 atoms leaving the torch through the exhausts, with respect to the total amount of Cu at the inlet (a), as well as the Cu species fraction at the sampler orifice (b), for different carrier gas flow rates ranging from 0.4 to 1.6 L/min. The fraction of Cu^{2+} ions is not shown in Figure 8a, because it is only on the order of 10^{-5}–10^{-6}, decreasing with flow rate. Again the sum of the three curves in Figure 8a is always equal to 100%, as the total amount of Cu in the torch, either as Cu^0 atoms or Cu^+ ions

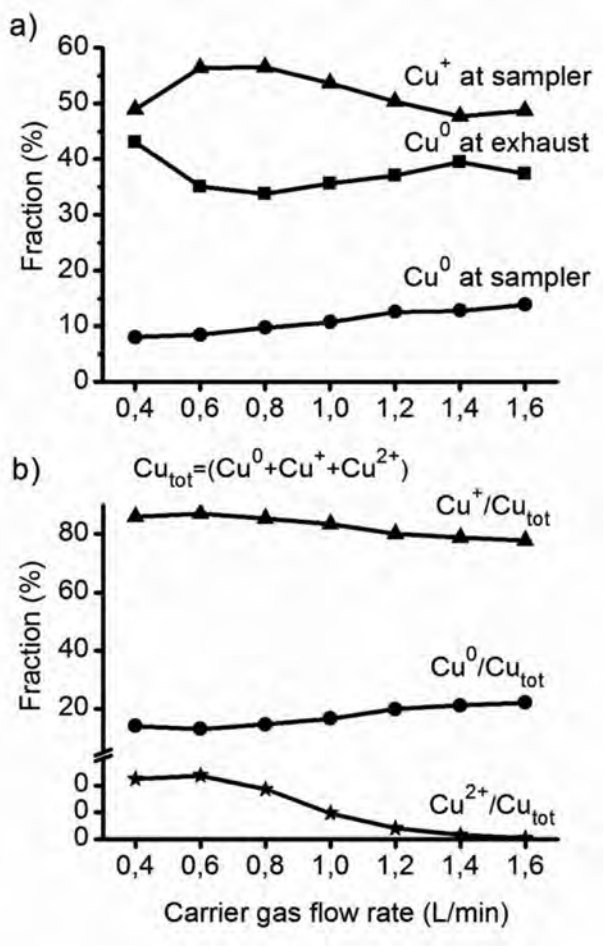

Figure 8. (a) Fraction of Cu^0 and Cu^+ at the sampler and fraction of Cu^0 leaving at the exhausts, with respect to the total amount of Cu at the inlet, and (b) fractions of Cu^0, Cu^+, and Cu^{2+} at the sampler orifice, with respect to the total amount of Cu passing through the sampler, for different carrier gas flow rates.

(and Cu^{2+} ions) must either leave the torch through the sampler orifice or the exhausts.

Figure 8a indicates that the fraction of Cu^+ ions which pass through the sampler orifice increases upon increasing the gas flow rate from 0.4 to 0.6–0.8 L/min, followed by a drop for higher gas flow rates. The fraction of Cu^0 atoms entering the sampler orifice slightly increases in the entire range of flow rates, and the fraction of Cu^0 atoms leaving the torch through the exhausts decreases from 0.4 to 0.6–0.8 L/min, followed by a small increase. This means that a carrier gas flow rate of 0.6–0.8 L/min yields a maximum transport efficiency, because it leads to a maximum in the fraction of Cu^+ ions reaching the sampler (56%) and at the same time to a minimum of Cu^0 atoms wasted at the exhausts (33%). The maximum of Cu exiting through the exhausts (43%) occurs at the minimum flow rate of 0.4 L/min.

The maximum and minimum in the fractions of Cu^+ ions at the sampler and Cu atoms at the exhausts, respectively, indicate that rising the carrier gas flow rate above the transition flow rate and up to 0.8 L/min shifts the sample more forward along the axis, which leads to a later evaporation, resulting in more species flowing toward the sampler than to the exhausts. However, a further increase in the gas flow rate at a fixed applied power leads to a drop in the plasma temperature and

DOI: 10.1021/acs.analchem.6b01189
Anal. Chem. 2016, 88, 8005–8018

thus in the ion number densities.[42] In general, around 60−65% of the Cu sample will pass through the sampler, with a dominant contribution from the Cu^+ ions (between 47% and 56%). Indeed, it is clear from Figure 8b that at all flow rates investigated, the majority of the Cu entering the sampler orifice will be Cu^+ ions. The Cu^{2+} ions form only a very minor fraction of the amount of Cu entering the sampler orifice.

In Figure 9, we show the fractions of Cu^+ ions at the sampler orifice, taken within 0.05 mm from the center, with respect to

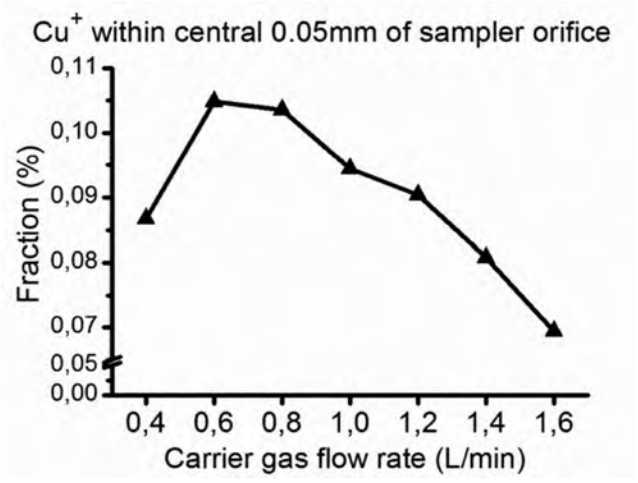

Figure 9. Fraction of Cu^+ ions passing through the central 0.05 mm of the sampler orifice, with respect to the total amount of Cu at the inlet, for different carrier gas flow rates.

the total amount of Cu at the inlet, for different carrier gas flow rates ranging from 0.4 to 1.6 L/min. It appears that increasing the carrier gas flow rate from 0.6 to 1.6 L/min results in about 35% lower transport of Cu^+ ions through the central 0.05 mm of the orifice. This drop is more pronounced than what is illustrated in Figure 8a, as only the very central region of the sampler orifice is considered here. Note that this 35% drop does not yet give information about the drop to be expected in the mass spectrum, as the effect of the ions passing through the skimmer and the rest of their journey inside the mass spectrometer is not yet accounted for.

Figure 10 presents more details about the changes occurring upon increasing the carrier gas flow rate, for 3 different values of the flow rate. The black contours (again plotted in the same scale for the three figures, ranging from 300 K to 10 000 K) show how the temperature profiles change when varying the carrier gas flow rate. It is clear that the area contained within the highest temperature contour line (corresponding to the area in the plasma above 10 000 K) becomes smaller and is further away from the central axis upon increasing gas flow rate. This raises the length of the cool central channel inside the torch, as is seen from Figure 10. Therefore, the analyte evaporation, atomization, and ionization processes will be strongly shifted downstream when the carrier gas flow rate increases. A shift of ∼12 mm along the axis is observed between a carrier gas flow rate of 0.4 and 0.8 L/min and a further shift of 10 mm occurs from 0.8 to 1.6 L/min. This is not only due to the higher transport velocity of the carrier gas in the ICP but in particular also due to the relatively large downstream shift of the plasma boundary (as indicated by the contour lines) and the lower maximum temperature due to the larger amount of cold gas volume injected. In fact, varying the flow rate from 0.4

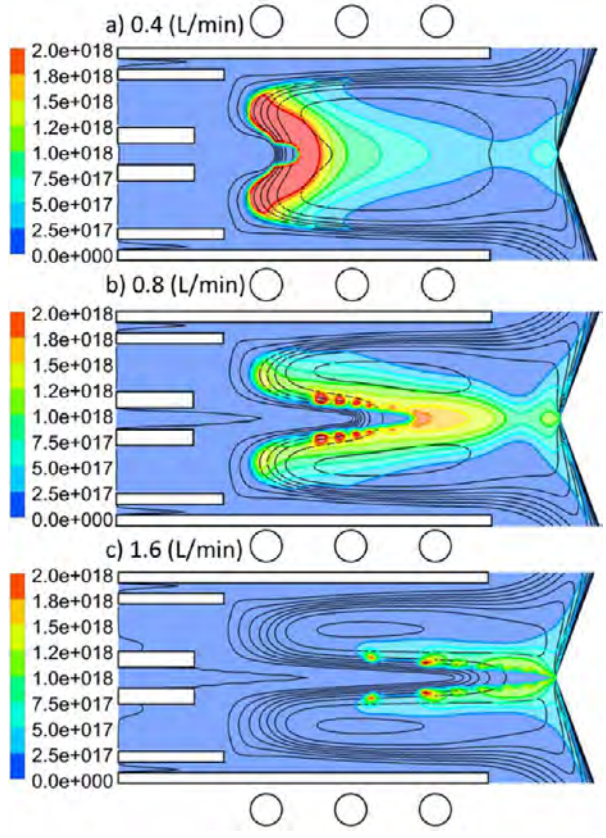

Figure 10. 2D profiles of Cu^+ number density at different carrier gas flow rate of (a) 0.4, (b) 0.8, and (c) 1.6 L/min as well as plasma temperature profiles (black contours) ranging from 300 to 10 000 K.

to 0.8 L/min (corresponding to a rise of 0.4 L/min), as seen in Figures 10a to 8b, results in a longer shift than further increasing the flow rate to 1.6 L/min, which corresponds to a rise of 0.8 L/min (cf. Figure 10b to 10c). This explains why the highest Cu^+ fraction at the sampler is predicted around 0.6−0.8 L/min. A further shift to the sampler upon further increasing the flow rate does not help, as the temperature drops by loading too much Ar to the plasma.

It is also apparent from Figure 10 that the ion cloud size changes significantly for the 3 different cases. As mentioned above, at the lower carrier gas flow rates, the ionization occurs earlier and the cloud expands more in the radial direction, while at the higher flow rates, the ion cloud is smaller and closer to the sampler. The reduction in ion cloud size upon increasing carrier gas flow rate was also reported by side-on fluorescence images of barium species.[25] In fact, the size of the ion cloud depends also on the composition of the sample particle,[21] which is of course not yet included in our present model. When the ion cloud size is large due to more radial diffusion, it will be beneficial to shift the ion cloud toward the sampler by increasing the carrier gas flow rate (see Figure 10a,b). Indeed, the detection efficiency in ICPMS is the best when the diffusion of analyte ions at the position of the MS sampler is limited, as was also reported in ref 18. Furthermore, the plasma temperature in the analyte−plasma interaction region has to be as high as possible to guarantee the most effective atomization and ionization. This explains why further increasing the carrier gas flow rate above 0.8 L/min does not increase the fraction of Cu^+ ions at the sampler.

DOI: 10.1021/acs.analchem.6b01189
Anal. Chem. 2016, 88, 8005−8018

A downstream shift in analyte vaporization, atomization, and ionization upon rising flow rate was also observed in experiments.[3,18,25] Indeed, in ref 25 a downstream shift of ~10 mm for a carrier gas flow rate rising from 0.87 until 1.52 L/min was reported, for an inlet diameter of 1.5 mm, and in ref 3, an increase of the carrier gas flow rate from 0.8 L/min to 1.0 L/min caused a 7 mm downstream shift in the position at which the particles of 13 μm diameter were completely desolvated. Shan and Mostaghimi also indicated that the height of complete desolvation increases linearly with an increase of the carrier gas flow rate.[37] By means of OES with end-on and side-on observation of the plasma, Niemax et al. determined the location of atomization in the ICP and the spatial distribution of diffused analyte ions at positions where the MS interface is typically placed in ICPMS. They report a shift of 25 mm for a rise in carrier gas flow rate from 0.25 to 0.5 L/min. They indicated that both a downstream shift of the atomization and a high temperature can be achieved by using injectors with a small inner diameter (1 mm) and higher injector gas flow rates.[18,19] It is important to realize that, compared to aerosol droplet introduction, dry particles as, for example, produced by LA of solid samples will start to evaporate earlier when they penetrate into the ICP. Consequently, analyte diffusion begins further upstream in the ICP and the ion cloud will be larger at the position of the sampler than with aerosol droplets, thus decreasing the analyte ion detection efficiency. In order to increase the ion detection efficiency of LA-ICPMS, the plasma boundary position has to be shifted downstream, e.g., by increasing the carrier gas flow rate.[18]

Although the lowest carrier gas flow rate of 0.4 L/min (Figure 10a) leads to a large ion cloud early in the plasma, which is not beneficial for the detection efficiency, the maximum Cu^+ ion density is here much higher than for the other gas flow rates, i.e., 5.3×10^{18} m^{-3} (thus significantly larger than the maximum of the color scale), while it is 3.2×10^{18} m^{-3} and 2.4×10^{18} m^{-3} for the carrier gas flow rates of 0.8 and 1.6 L/min, respectively. This is of course also attributed to the higher plasma temperature at the lower flow rate (cf. above).

From both Figures 8 and 10, we can conclude that a carrier gas flow rate between 0.6 and 0.8 L/min is the optimum range for the current setup. Indeed, according to Figure 8a, the carrier gas flow rate of 0.6−0.8 L/min yields the highest fraction of Cu^+ ions at the sampler, and Figure 10b shows that at this flow rate the ion cloud is properly shifted toward the sampler. A further increase is not recommended because the temperature and ion density drop along the axis and this condition cannot provide sufficient heat to complete the desolvation and ionization (see Figure 10c). Furthermore, the analyte atoms will diffuse and become ionized, forming ion vapor clouds with increasing diameter downstream the plasma.[19] It should be realized that early evaporation and more radial expansion from the central axis, which is the case for the flow rates below 0.6 L/min in this study, may cause that some part of the sample ions does not reach the sampler orifice, which thus represents a loss.[19] Moreover, even if they are not lost, it may cause a delay in detection time, for example, when different elements in an expanded ion cloud are carried by different Ar path lines, which have different axial velocity along the torch, especially when arriving at the sampler, as was observed in ref 56.

CONCLUSION

We studied the transport, evaporation, and ionization of copper particles through an inductively coupled plasma, connected to the sampling cone of a mass spectrometer, by means of a computational model. Our aim is to obtain a better insight into the particle transport, evaporation, and ionization inside the ICP torch and to optimize the transport efficiency of the injected sample material through the ICP and the sampling cone. This model provides us, for the first time, detailed profiles of all atomic and ionic species inside the torch as well as at the sampler orifice. Our calculations show that the particles follow different path lines of the Ar gas flow in the torch and expand differently in the radial direction from the central axis, depending on their exact position of injection.

The 2D profiles of the various ion number densities provide us the axial and radial position at which the ionization occurs, which depends on the plasma temperature along the torch. They also show to what extent the ion cloud moves in the radial direction and deviates from the central axis. In a group of particles injected from the central inlet, the ones introduced near the center of the inlet (on-axis) move in a more straight line along the torch and experience a later evaporation and ionization compared with the particles introduced near the outer region of the inlet (off-axis). Thus, on-axis injection reduces the probability of losing the sample inside the torch or the occurrence of a detection delay, by preventing the particles from early radial expansion inside the torch. Also, it ensures less expansion in the first vacuum stage and therefore a lower amount of sample lost through the skimmer.

Besides the 2D density profiles of the various ions and atoms, we also focused especially on their fluxes at the position of the sampler orifice. More specifically, we calculated the fraction of Cu^+ and Cu^{2+} ions and Cu^0 atoms entering the sampling cone as well as the fraction of Cu^0 atoms leaving the torch through the exhausts, for both on-axis and off-axis injection, and for a range of different applied powers and carrier gas flow rates, to determine the transport efficiency of the sample material at these different conditions. As mentioned above, on-axis sample injection yields a significantly higher fraction of Cu^+ ions entering the sampler orifice, i.e., 90% vs 48% in the case of off-axis injection.

The effect of applied power was studied in the range of 600−1600 W. We showed that the entire ion cloud moves upstream inside the torch upon increasing applied power up to 1000 W, but for higher power values, a secondary maximum is observed near the sampler, and this explains why the Cu^+ fraction entering the sampler orifice first slightly decreases (up to 1000 W) and then slightly increases upon increasing power. Our calculations predict that for the conditions under study (i.e., geometrical setup, Ar gas flow rates and copper mass loading flow rate), a power of around 1400 W is preferable to move the ion cloud close to the sampler.

Furthermore, increasing the carrier gas flow rate in the range between 0.4 and 1.6 L/min leads to cooling of the central plasma temperature. As a consequence, the position of maximum ionization moves downstream to the sampler. We showed that a rise from 0.4 to 0.6−0.8 L/min leads to a higher ion density at the sampler, with the highest Cu^+ fraction entering the sampler at 0.6−0.8 L/min. Taking into account the amount of gas consumption, a further increase in flow rate is not recommended as it does not improve the Cu^+ ion density at the sampler, because of cooling of the plasma inside the torch.

DOI: 10.1021/acs.analchem.6b01189
Anal. Chem. 2016, 88, 8005−8018

When considering the central 0.05 mm of the sampler orifice, a 35% drop in transport efficiency of the Cu^+ ions is calculated upon increasing the carrier gas flow rate from 0.6 to 1.6 L/min. However, the latter does not yet give information about the drop to be expected in the mass spectrum, because the next stages of the ion journey inside the MS until the detection point are not yet accounted for.

Our calculated results, especially for the effect of power and carrier gas flow rates, are compared with experiments from the literature as much as possible, and good qualitative agreement is reached. In general, we may conclude from our calculations that about 50% of the injected copper will pass through the sampling cone. This value will be slightly higher with increasing power and carrier gas flow rate up to 0.8 L/min. However, when all particles can be injected on-axis, the transport efficiency rises to about 90%. This suggests that one should be able to improve the transport efficiency by using a narrower central gas inlet, where all the sample material is injected close to on-axis.

AUTHOR INFORMATION

Corresponding Author

*E-mail: maryam.aghaei@uantwerpen.be.

Notes

The authors declare no competing financial interest.

ACKNOWLEDGMENTS

The authors gratefully acknowledge financial support from the Fonds voor Wetenschappelijk Onderzoek (FWO), Grant Number 6713. The computational work was carried out using the Turing HPC infrastructure at the CalcUA core facility of the Universiteit Antwerpen (UA), a division of the Flemish Supercomputer Center VSC, funded by the Hercules Foundation, the Flemish Government (department EWI), and the UA.

REFERENCES

(1) Houk, R. S. *Anal. Chem.* **1986**, *58* (1), 97A−105A.
(2) Hieftje, G. M.; Malmstadt, H. V. *Anal. Chem.* **1968**, *40*, 1860−1867.
(3) Olesik, J. W. *Appl. Spectrosc.* **1997**, *51*, 158−175.
(4) Olesik, J. W.; Hobbs, S. E. *Anal. Chem.* **1994**, *66*, 3371−3378.
(5) Olesik, J. W.; Kinzer, J. A. *Spectrochim. Acta, Part B* **2006**, *61*, 696−704.
(6) Kinzer, J. A. *Inductively Coupled Plasma Spectrometry (CE−ICP): Elemental speciation and fundamental studies of matrix effects in the ICP.* Ph.D. Thesis, The Ohio State University, Columbus, OH, 1997.
(7) Lazar, A. C.; Farnsworth, P. B. *Appl. Spectrosc.* **1999**, *53*, 465−470.
(8) Lazar, A. C.; Farnsworth, P. B. *Appl. Spectrosc.* **1997**, *51*, 617−624.
(9) Olesik, J. W.; Smith, L. J.; Williamsen, E. J. *Anal. Chem.* **1989**, *61*, 2002−2008.
(10) Monnig, C. A.; Koirtyohann, S. R. *Anal. Chem.* **1985**, *57*, 2533−2576.
(11) Winge, R. K.; Crain, J. S.; Houk, R. S. *J. Anal. At. Spectrom.* **1991**, *6*, 601−604.
(12) Houk, R. S.; Winge, R. K.; Chen, X. *J. Anal. At. Spectrom.* **1997**, *12*, 1139−1148.
(13) Aeschliman, D. B.; Bajic, S. J.; Baldwin, D. P.; Houk, R. S. *J. Anal. At. Spectrom.* **2003**, *18*, 1008−1014.
(14) Perdian, D. C.; Bajic, S. J.; Baldwin, D. P.; Houk, R. S. *J. Anal. At. Spectrom.* **2008**, *23*, 325−335.
(15) Jorabchi, K.; Brennan, R. G.; Levine, J. A.; Montaser, A. *J. Anal. At. Spectrom.* **2006**, *21*, 839−846.
(16) Groh, S.; Garcia, c. C.; Murtazin, A.; Horvatic, V.; Niemax, K. *Spectrochim. Acta, Part B* **2009**, *64*, 247−254.
(17) Groh, S.; Diwakar, P.; Garcia, C. C.; Murtazin, A.; Hahn, D. W.; Niemax, K. *Anal. Chem.* **2010**, *82*, 2568−2573.
(18) Murtazin, A.; Groh, S.; Niemax, K. *Spectrochim. Acta, Part B* **2012**, *67*, 3−16.
(19) Niemax, K. *Spectrochim. Acta, Part B* **2012**, *76*, 65−69.
(20) Gschwind, S.; Flamigni, L.; Koch, J.; Borovinskaya, O.; Groh, S.; Niemax, K.; Günther, D. *J. Anal. At. Spectrom.* **2011**, *26*, 1166−1174.
(21) Flamigni, L.; Koch, j.; Günther, D. *Spectrochim. Acta, Part B* **2012**, *76*, 70−76.
(22) Koch, J.; Günther, D. *Appl. Spectrosc.* **2011**, *65*, 155−162.
(23) Blades, M. W.; Horlick, G. *Spectrochim. Acta, Part B* **1981**, *36*, 861−880.
(24) Chan, G. C. Y.; Hieftje, G. M. *J. Anal. At. Spectrom.* **2009**, *24*, 439−450.
(25) Mills, A. A.; Macedone, J. H.; Farnsworth, P. B. *Spectrochim. Acta, Part B* **2006**, *61*, 1039−1049.
(26) Horner, J. A.; Lehn, S. A.; Hieftje, G. M. *Spectrochim. Acta, Part B* **2002**, *57*, 1025−1042.
(27) Miller, R. C.; Ayen, R. J. *J. Appl. Phys.* **1969**, *40*, 5260−5273.
(28) Barnes, R. M.; Schleicher, R. G. *Spectrochim. Acta, Part B* **1975**, *30*, 109−134.
(29) Boulos, M. I. *IEEE Trans. Plasma Sci.* **1978**, *6*, 93−106.
(30) Mostaghimi, J.; Pfender, E. *Plasma Chem. Plasma Process.* **1984**, *4*, 199−217.
(31) Mostaghimi, J.; Proulx, P.; Boulos, M. I. *Numer. Heat Transfer* **1985**, *8*, 187−201.
(32) Yang, P.; Barnes, R. M.; Mostaghimi, J.; Boulos, M. I. *Spectrochim. Acta, Part B* **1989**, *44*, 657−666.
(33) Mostaghimi, J.; Proulx, P.; Boulos, M. I.; Barnes, R. M. *Spectrochim. Acta, Part B* **1985**, *40*, 153−166.
(34) Benson, C. M.; Gimelshein, S. F.; Levin, D. A.; Montaser, A. *Spectrochim. Acta, Part B* **2001**, *56*, 1097−1112.
(35) Benson, C. M.; Zhong, J.; Gimelshein, S. F.; Levin, D. A.; Montaser, A. *Spectrochim. Acta, Part B* **2003**, *58*, 1453−1471.
(36) Horner, J. A.; Hieftje, G. M. *Spectrochim. Acta, Part B* **1998**, *53*, 1235−1259.
(37) Shan, Y.; Mostaghimi, J. *Spectrochim. Acta, Part B* **2003**, *58*, 1959−1977.
(38) Spencer, R. L.; Krogel, J. T.; Palmer, J.; Payne, A.; Sampson, A.; Somers, W.; Woods, C. N. *Spectrochim. Acta, Part B* **2009**, *64*, 215−221.
(39) Spencer, R. L.; Taylor, N.; Farnsworth, P. B. *Spectrochim. Acta, Part B* **2009**, *64*, 921−924.
(40) Lindner, H.; Bogaerts, A. *Spectrochim. Acta, Part B* **2011**, *66*, 421−431.
(41) Aghaei, M.; Lindner, H.; Bogaerts, A. *J. Anal. At. Spectrom.* **2012**, *27*, 604−610.
(42) Aghaei, M.; Lindner, H.; Bogaerts, A. *Spectrochim. Acta, Part B* **2012**, *76*, 56−64.
(43) Aghaei, M.; Lindner, H.; Bogaerts, A. *J. Anal. At. Spectrom.* **2013**, *28*, 1485−1492.
(44) Aghaei, M.; Flamigni, L.; Lindner, H.; Günther, D.; Bogaerts, A. *J. Anal. At. Spectrom.* **2014**, *29*, 249−261.
(45) Aghaei, M.; Bogaerts, A. *J. Anal. At. Spectrom.* **2016**, *31*, 631−641.
(46) Lindner, H.; Murtazin, A.; Groh, S.; Niemax, K.; Bogaerts, A. *Anal. Chem.* **2011**, *83*, 9260−9266.
(47) D'Ans, J.; Lax, E. *Taschenbuch für Chemiker und Physiker, Band 1; Physikalischchemische Daten*, 4th ed.; Springer-Verlag: Berlin, Germany, 1992.
(48) Murphy, A. B.; Arundelli, C. J. *Plasma Chem. Plasma Process.* **1994**, *14* (4), 451−490.
(49) Murphy, A. B. *IEEE Trans. Plasma Sci.* **1997**, *25*, 809−814.
(50) Chen, W. L. T.; Heberlein, J.; Pfender, E.; Pateyron, B.; Delluc, G.; Elchinger, M. F. *Plasma Chem. Plasma Proc.* **1995**, *15* (3), 559−579.

DOI: 10.1021/acs.analchem.6b01189
Anal. Chem. 2016, 88, 8005−8018

(51) Yang, P.; Horner, J. A.; Sesi, N. N.; Hieftje, G. M. *Spectrochim. Acta, Part B* **2000**, *55*, 1833−1845.
(52) Pupyshev, A. A.; Lutsak, A. K. *J. Anal. Chem.* **2002**, *57*, 672−680.
(53) Mostaghimi, J.; Proulx, P.; Boulos, M. I.; Barnes, R. M. *Spectrochim. Acta, Part B* **1985**, *40*, 153−166.
(54) Murphy, A. B. *J. Phys. D: Appl. Phys.* **1996**, *29*, 1922−1932.
(55) Borovinskaya, O.; Aghaei, M.; Flamigni, L.; Hattendorf, B.; Tanner, M.; Bogaerts, A.; Günther, D. *J. Anal. At. Spectrom.* **2014**, *29*, 262−271.
(56) Lindner, H. *Untersuchungen zur Partikelverteilung und -zusammensetzung beim Laserabtrag*. Thesis, Universität Dortmund, Dortmund, Germany, 2004.
(57) Pupyshev, A. A.; Semenova, E. V. *Spectrochim. Acta, Part B* **2001**, *56*, 2397−2418.
(58) Radicic, W. N.; Olsen, J. B.; Nielson, R. V.; Macedone, J. H.; Farnsworth, P. B. *Spectrochim. Acta, Part B* **2006**, *61*, 686−695.

DOI: 10.1021/acs.analchem.6b01189
Anal. Chem. 2016, 88, 8005−8018